ELSEVIER

Contents lists available at ScienceDirect

Earth and Planetary Science Letters

journal homepage: www.elsevier.com/locate/epsl



Insights into the last 100 ky of geomagnetic field variability using numerical dynamo simulations

Stephen J. Mason a,*, Christopher J. Davies a, Andrew T. Clarke a, Catherine G. Constable b

- ^a School of Earth and Environment, University of Leeds, Leeds, LS2 9JT, UK
- b Institute of Geophysics & Planetary Physics, Scripps Institution of Oceanography, University of California San Diego, La Jolla, CA, USA

ARTICLE INFO

Editor: H. Thybo

Dataset link: https://earthref.org/ERDA/2744/

Keywords: Geomagnetic field Polarity excursions Numerical modelling Paleomagnetic timescales

ABSTRACT

Recent observational models of the paleomagnetic field have revealed new details about geomagnetic field variability, which have yet to be adequately explored in numerical dynamo simulations. Here we present results from a new suite of dynamo simulations with computationally accessible rotating rates and diffusivities, an Earth-like magnetic Reynolds number, and a force balance that is consistent with the expected regime of the geodynamo, allowing comparison of simulated data and observational models. We find that such simulations are able to simultaneously reproduce the observed extreme rates of change in intensity and direction as well as the general amplitude of field variability over the last 100 ky, if the mean dipolarity is in the range 0.4-0.5. We use the paleosecular variation (PSV) index to identify a broad spectrum of polarity excursions and show that the PSV index is closely linked to the dipolarity of the simulation. Simulated excursional events are mostly associated with a decrease in the axial dipole moment with generally modest changes in dipole tilt. The excursions range from global events characterised by a reduction in the field contribution from solely the axial dipole component and a decrease in mean VDM in the manner of the Laschamp excursion, to localised events with anomalous activity in small regions reminiscent of the Mono Lake/Auckland excursion. Global events are generally longer than regional excursions, and reflect a drop in the total magnetic energy of the dynamo.

1. Introduction

A dynamo process occurring in Earth's liquid outer core is responsible for the generation of the geomagnetic field. The time-dependent nature of this field has been well-established through analysis of historical (Jackson et al., 2000) and paleomagnetic records (e.g. Merrill et al., 1998; Ogg, 2020), which have revealed that changes occur on timescales ranging from seconds to years to millennia (Panovska et al., 2018b; Bono et al., 2019). Numerical dynamo simulations routinely produce dipoledominated fields (e.g. Wicht and Sanchez, 2019), a configuration that the geomagnetic field is thought to have adopted over much of its history (e.g. Biggin et al., 2020), as well as spontaneous polarity reversals (e.g. Glatzmaier and Roberts, 1995; Olson and Amit, 2014). Furthermore these simulations can reproduce the large-scale morphological features and temporal variability of the present geomagnetic field (e.g. Christensen et al., 2010; Mound and Davies, 2023), and can also match the primary field features of the past 10 My (Meduri et al., 2021). Here we address an intermediate timescale, 0 - 100 ka, which has received little attention owing to a lack of observational constraints on the global field behaviour. This situation has now changed, with a recent series of global time-dependent spherical harmonic representations of the field in the $0-100~\rm ka$ interval enabling direct comparisons with the outputs of geodynamo simulations.

Recent observational models covering various periods within the last 100 ky (Panovska et al., 2018b; Korte et al., 2019a; Osete et al., 2020; Liu et al., 2020; Panovska et al., 2021) have identified several field features that are not captured in the 400-yr historical record. During this interval there have been 4-5 polarity excursions, each with varying duration and features. Models such as GGF100k (Panovska et al., 2018b) and LSMOD.2 (Korte et al., 2019a) have found the Laschamp excursion, the most prominent excursion of the last 100 ky, to be a global event lasting approximately 1800 years characterised by a decrease in virtual dipole moment (VDM) and an increase in directional variability (Panovska et al., 2019; Korte et al., 2019b). Notably, the decrease in VDM is caused by a drastic reduction in the axial dipole contribution, whilst the size of equatorial dipole contributions remains unchanged (Korte et al., 2019b). Other excursions are shorter (Mono Lake/Auckland lasts only 1040 years), display less prominent changes in field

E-mail address: s.mason1@leeds.ac.uk (S.J. Mason).

^{*} Corresponding author.

strength and are not global in extent, with large intensity and directional variations focused in smaller, more localized regions.

Observations in the period 0 - 100 ka also reveal rates of change in both intensity (Shaar et al., 2016; Ben-Yosef et al., 2017; Osete et al., 2020) and direction (Davies and Constable, 2020; Maffei et al., 2021) that are up to ~10 times faster than those seen in the historical record. Direct paleomagnetic observations from the first millennium BCE, together with tight chronological constraints, have been interpreted as intensity changes reaching 0.75-1.5 μ T yr⁻¹ (Ben-Yosef et al., 2017) (compared to values of $0.12 \,\mu\text{T yr}^{-1}$ for the historical field). Such changes are spatially localised (Davies and Constable, 2017) and are associated with regions of strong field (Constable and Davies, 2024). In global paleomagnetic field models much lower values are found for rates of intensity change (maxima of around 0.3 μ T yr⁻¹) but these almost certainly underestimate the rates of change because of the smoothing effects inherent in building global models. However, rapid directional changes are found in time-varying models associated with anomalously weak fields near excursions and can exceed 1° yr-1, compared to average values for the historical field of 0.1°yr⁻¹ (Constable and Davies, 2024).

Geodynamo simulations provide additional information that complements paleomagnetic data. Simulations can run with a much higher spatial and temporal resolution than available in observational models, whilst running for longer timescales that allow for the occurrence of multiple excursions and reversals. In addition, velocity and magnetic fields are generated throughout the core, allowing the dynamics of the dynamo process to be probed directly. The disadvantage is that direct numerical simulations are currently unable to run at the physical conditions of Earth's core. This issue can be best addressed by setting up simulations that have the right balance of terms in the governing equations. In the magnetic induction equation this amounts to requiring that the magnetic Reynolds number $Rm \sim 1000$, which is readily achieved in current simulations (Aubert et al., 2017; Schaeffer et al., 2017; Nakagawa and Davies, 2022). In the momentum equation, theory (Davidson, 2013; Calkins, 2018) and simulations (Dormy, 2016; Schaeffer et al., 2017; Aubert, 2019) indicate that the dominant balance in Earth's core is Quasi-Geostrophic (QG), with a secondary Magnetic-Archimedean-Coriolis (MAC) balance. This QG-MAC balance can be achieved in simulations conducted at moderate physical conditions, though with substantial residual contributions from viscous and inertial terms (Schwaiger et al., 2019; Nakagawa and Davies, 2022). With careful selection of control parameters it is possible to move to more extreme physical conditions preserving high Rm and the QG-MAC balance while reducing the residual contributions to the force balance (Aubert et al., 2017).

Previous dynamo studies have considered specific aspects of paleofield behaviour contained within the 0 - 100 ka interval. Excursions have been found in a number of simulations (e.g. Olson et al., 2009; Lhuillier et al., 2013), but their properties have not been compared to the detailed records now available from global field models (Panovska et al., 2019; Liu et al., 2020). Moreover, while simulations are known to produce a diverse range of reversal behaviour (Olson et al., 2009, 2011), the range of excursional behaviour and its correspondence with observations over the 0-100 ka period has not been investigated. Rapid rates of change have been directly compared between simulations and observations. Davies and Constable (2018) found maximum rates of intensity change reaching 0.75 μT yr⁻¹, in line with values of 0.75-1.5 $\mu T \text{ yr}^{-1}$ found in the Levantine region around 1000 BCE (Ben-Yosef et al., 2017; Livermore et al., 2021). Davies and Constable (2020) found maximum directional changes of $\sim 10^{\circ} \text{ yr}^{-1}$ in simulations, which are broadly consistent with observed values. However, few of the simulations used to investigate rapid field changes have achieved the high Rm QG-MAC dynamics thought to be relevant to Earth's core.

In this paper we compare existing observational field models spanning the 0-100 ka interval to a suite of 20 new dynamo simulations. The simulations span a range of Ekman number $E=1.5\times 10^{-5}-10^{-3}$, magnetic Prandtl number Pm=4-50 and Rayleigh number $Ra=1.5\times 10^{-5}$

 $4.8 \times 10^5 - 2.82 \times 10^8$ (parameters are defined precisely below). These values are still far from the conditions of Earth's core. To mitigate this issue we consider only simulations that achieve high Rm(>770) and QG-MAC balance as measured by a magnetic to kinetic energy ratio exceeding 1. Section 2 describes the simulations and metrics used to quantitatively compare simulated outputs to field models. In Section 3 we first analyze the rates of change of the intensity and direction as well as the general variability of the simulated field, finding observed pale-osecular variation is matched when the mean dipolarity $f_{dip} = 0.4 - 0.5$. We then explore field behaviour during polarity excursions. Discussion and conclusions are presented in Section 4.

2. Methods

2.1. Dynamo simulations

We study thermally-driven convection and dynamo action in a rotating spherical shell, numerically solving the governing equations using the Leeds Dynamo Code (Willis et al., 2007). The code solves the standard equations governing conservation of mass, momentum, energy and magnetic field for an electrically conducting fluid contained within a rotating spherical shell. The non-dimensional parameters in the governing equations are

$$Ra = \alpha g_o Q D^4 / 4\pi r_o k \nu \kappa, \tag{1}$$

$$Ek = \nu/\Omega D^2,\tag{2}$$

$$Pm = \nu/\eta,\tag{3}$$

$$Pr = v/\kappa,$$
 (4)

where α is the thermal expansion coefficient, g_o is the gravity at the outer radius of the shell, Q is the convective heat flow, k is thermal conductivity, v is kinematic viscosity, $D = r_o - r_i$ is the thickness of the spherical shell where r_o is the outer boundary and r_i is the inner boundary, Ω is the rotation rate around the vertical $\hat{\mathbf{z}}$ -axis, η is the magnetic diffusivity, and κ is the thermal diffusivity. Gravity varies linearly in radius, $\mathbf{g} = -g_o r/r_o \mathbf{e}_r$, where \mathbf{e}_r is the radial unit vector.

We have analysed a set of 20 simulations, with boundary conditions that are electrically insulating, no-slip and impenetrable at $r = r_i$ and r = r_{o} . Convection is thermally driven by homogeneous fixed-flux boundary conditions, with the dimensionless heat flux at the inner boundary $F_i = -1/r_i^2 \approx -3.4490$ and at the outer boundary $F_o = -1/r_o^2 = -0.4225$. A case summary is provided in Appendix A. 17 of the simulations are extended runs from those of Nakagawa and Davies (2022), as indicated by the LEDT prefix in Tables A.1-A.2, with new simulations indicated by the prefix LEDS. All simulations have a QG-MAC force balance as measured by the strong field parameter $\delta > 1$ (defined by Schwaiger et al. (2019), see Table A.1), magnetic Reynolds number $Rm = UD/\eta \sim \mathcal{O}(10^3)$ (where *U* is the characteristic velocity), and the ratio of magnetic to kinetic energy $E_{mag}/E_{kin} > 2$. The aspect ratio r_i/r_o is set to 0.35 throughout. The values of the other non-dimensional control parameters are within the ranges $4.8 \times 10^5 \le Ra \le 2.82 \times 10^8$, $1.5 \times 10^{-5} < Ek \le 10^{-3}$, $4 < Pm \le 50$, with Pr = 1 in all of our simulations. Spatial resolutions range from 96 to 256 radial gridpoints, with spherical harmonics for the angular coordinates truncated between degree 96 and 128, depending on the combination of non-dimensional parameters used.

All 20 simulations have had time integrations performed for at least 1 magnetic diffusion time, with transients excluded. As time t has been non-dimensionalised using the simulation diffusion timescale $\tau_m^d = D^2/\eta$, we have $t = \tau_m^d t_*$ where t_* is non-dimensional time. This is equivalent to $t = Rm_m \tau_m^a t_*$ where $\tau_m^a = D/U$ is the simulation advection timescale and $Rm_m = \tau_m^d/\tau_m^a$ is Rm of the simulation. Similarly Rm of the Earth is $Rm_E = \tau_E^d/\tau_E^a$. If we rescale to dimensional time using a diffusive timescale $(\tau_m^d = \tau_E^d)$ we obtain $t = \tau_m^d t_*$, and if we rescale using an advective timescale $(\tau_m^a = \tau_E^a)$ we obtain $t = Rm_m \tau_E^a t_*$, or equivalently

$$t = \tau_E^d t_* \frac{Rm_m}{Rm_E}. \tag{5}$$

Since both Rm_m and Rm_E are $\mathcal{O}(10^3)$, we take $Rm_m/Rm_E=1$, and as a result, $t=\tau_E^dt_*$ regardless of whether we choose to rescale to dimensional time using either a diffusive or advective timescale (see for example Davies and Constable (2014)). Using D=2264 km and a magnetic diffusivity of 1 m² s⁻¹ (Davies et al., 2015), we find one magnetic diffusion time is equivalent to approximately 162 ky of real time, allowing for comparison with paleofield observational models on multi-millennial timescales.

2.2. Paleomagnetic analysis

We make direct comparisons between dynamo simulations and two time-varying spherical harmonic paleomagnetic fields models, LSMOD.2 (Korte et al., 2019b) covering the time interval 30-50 ka, and GGF100k Panovska et al. (2018b) extending from 0-100 ka. The majority of the paleomagnetic data contributing to these models are derived from marine sediments but archeomagnetic and volcanic records also play a significant role, especially in calibrating the relative paleointensity variations from the sediment records. Details of the data compilations are provided in Brown et al. (2018) and Panovska et al. (2018a), respectively. Predictions from the spherical harmonic models as a function of time and space are used to produce paleofield diagnostics in the form of average and peak rates of change and of the paleosecular variation index (Panovska and Constable, 2017) as a function of time. These can be directly compared with products from the numerical simulations.

Following Davies and Constable (2018) at each time t we calculate Gauss coefficients from the poloidal magnetic field at the outer boundary of the model, from which the three components X, Y and Z of the local magnetic field vector \mathbf{B} are calculated on a 2° by 2° latitude–longitude grid at Earth's surface. We consider two values for ℓ_{max} , the maximum spherical harmonic truncation of the Gauss coefficients: $\ell_{max} = 5$ corresponding to the estimated resolution of the field models (Korte et al., 2019b; Panovska et al., 2019); $\ell_{max} = 12$ approximating the resolution that would be achieved with ideal data coverage. Differences between outputs obtained with the two truncations give an indication of the resolution-dependence of the results.

When calculating rates of change, following the notation of Panovska and Constable (2017) and Davies and Constable (2020), we define \mathbf{M}_V as the virtual dipole vector with amplitude \mathbf{M}_V equivalent to the VDM. Virtual dipole position $\hat{\mathbf{M}}_V$ with latitude λ_V and longitude ϕ_V is calculated from inclination I and declination D and then converted to unit vectors using

$$\hat{X}_V = \cos(\lambda_V)\cos(\phi_V), \ \hat{Y}_V = \cos(\lambda_V)\sin(\phi_V), \ \hat{Z}_V = \sin(\lambda_V).$$
 (6)

The rate of change of $\hat{\mathbf{M}}_V$ between times t and $t_1 = t + \Delta t$ is then given by

$$\frac{\partial \hat{\mathbf{M}}_V}{\partial t} = \frac{\arccos[\hat{X}_V(t)\hat{X}_V(t_1) + \hat{Y}_V(t)\hat{Y}_V(t_1) + \hat{Z}_V(t)\hat{Z}_V(t_1)]}{\Delta t}. \tag{7}$$

The rate of change of M_V is given by

$$\frac{\partial M_V}{\partial t} = \frac{M_V(t_1) - M_V(t)}{\Delta t},\tag{8}$$

where M_V is calculated from

$$M_V = \frac{4\pi a^3 \sqrt{1 + 3\cos^2(I)}B}{2\mu_0},\tag{9}$$

where *B* is the strength of the local field vector defined as $B = \sqrt{X^2 + Y^2 + Z^2}$, a = 6371 km is Earth's radius, and μ_0 is magnetic vacuum permeability.

To characterise the field morphology we use the dipolarity f_{dip} , the time-averaged ratio of the root mean square (RMS) dipole field strength to the total RMS field strength up to $\ell_{max}=12$ at the outer boundary

of the simulation (Christensen and Aubert, 2006). We have chosen to distinguish between simulations using the terminology 'reversing' and 'non-reversing' rather than 'dipolar' and 'multipolar', as it is unclear at what point a simulation is no longer classified as dipole-dominated. Other morphological characteristics that have been used to compare simulations to the historical field such as equatorial symmetry and flux concentration (Christensen et al., 2010) and the pattern of secular variation (Mound et al., 2015; Mound and Davies, 2023) are not robustly determined over the past 100 ky field. We discuss the compliance of the simulations with the criteria proposed by Christensen et al. (2010) in Section 3.1.

To characterise paleosecular variation we use the activity index $P_i(\lambda,\phi,t)$ of Panovska and Constable (2017), which measures the combined variation of field strength and direction. The activity index is useful because it can be calculated locally (at individual points in space and time) as well as globally (by averaging or integration) for individual data records, field models and dynamo simulations. At a latitude λ , longitude ϕ , and time t, P_i is defined as

$$P_i(\lambda, \phi, t) = \frac{(\pi/2 - |\lambda_V(\lambda, \phi, t)|) M_{V_0}}{\pi M_V(\lambda, \phi, t)},$$
(10)

where M_{V_0} is the time-averaged dipole moment. For a quantity $F(\lambda, \phi, t)$, we use the notation

$$\operatorname{mean}(F) \\
\lambda \phi t \tag{11}$$

and

$$\max_{\lambda,\phi,t}(F) \tag{12}$$

to denote the average and maximum values of F over the dimensions λ , ϕ and t respectively. For example, $\displaystyle\max_{\lambda,\phi}(M_V)(t)$ indicates a spatial average of $M_V(\lambda,\phi,t)$ over λ and ϕ , with the resulting output therefore being a function of t. For brevity, when calculating average or maximum values over only 1 or 2 dimensions, the remaining dimension(s) of the output are not always shown i.e. $\displaystyle\max_{\lambda}(M_V)$.

The activity index can be used to establish the attributes of magnetic field excursions. Based on results from paleofield models (Panovska et al., 2019) we distinguish between *global* and *regional* excursions. Conventional definitions of excursions in the paleomagnetic literature use a VGP latitude of < 45° and/or field strength below half of the long-term average, and from these values Panovska and Constable (2017) proposed that geomagnetic excursions are characterized by mean values of the activity index that are greater than 0.5, and made a clear distinction between regional and global excursions.

To define the times t_s and t_e when a global excursion starts and ends, following Panovska and Constable (2017) and Panovska et al. (2019), we use the conditions

$$\underset{\lambda,\phi}{\mathrm{mean}}(P_i)(t_s) > 0.5 \quad \text{and} \quad \underset{\lambda,\phi}{\mathrm{mean}}(P_i)(t_e) < 10^{\underset{i}{\mathrm{mean}}\left(\log_{10}\underset{\lambda,\phi}{\mathrm{mean}}(P_i)\right)}, \tag{13}$$

respectively, the latter of which is approximately 0.1 in all of our simulations. To define the time t_e at which a global excursion ends we have accounted for the fact that the dipole field can take an extended period to recover to its pre-excursion strength (Panovska et al., 2019). When applied to the paleomagnetic field models, the Laschamp excursion is the only global excursional event of the past 100 ky (Panovska et al., 2019).

We define a regional excursion as an event that starts and ends when

$$\max_{\lambda,\phi}(P_i)(t_s) > 0.5 \quad \text{and} \quad \max_{\lambda,\phi}(P_i)(t_e) < 0.5, \tag{14}$$

respectively. By this definition the Mono Lake/Auckland excursion is a regional excursion, as P_i exceeds 0.5 in Northern Africa/Eastern Europe

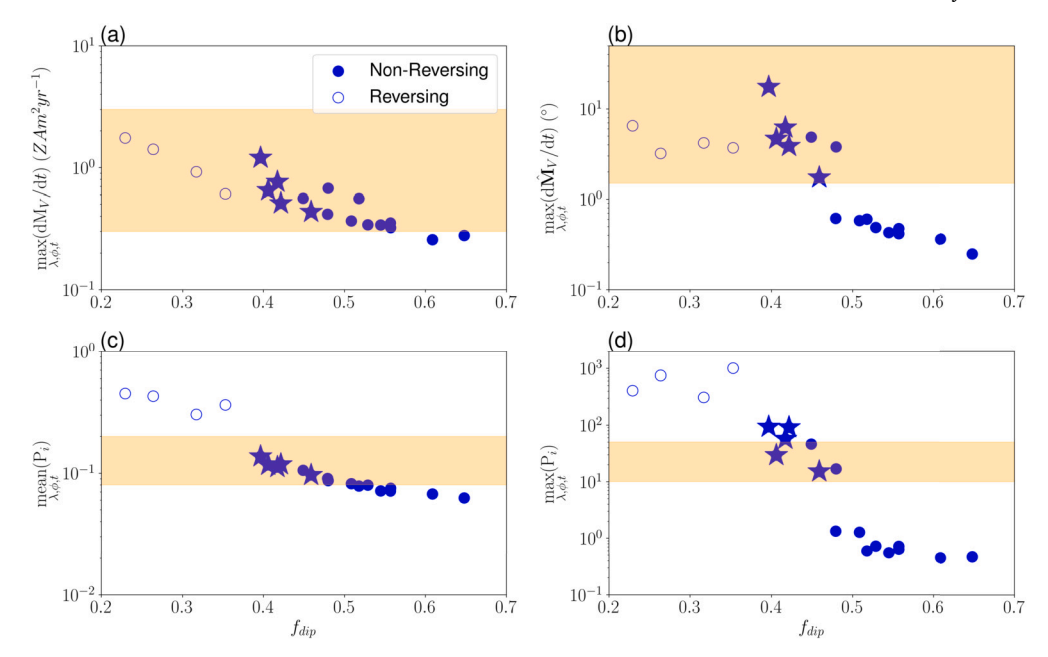


Fig. 1. (a) $\max_{\lambda,\phi,l}(dM_V/dt)$, (b) $\max_{\lambda,\phi,l}(d\hat{M}_V/dt)$, (c) $\max_{\lambda,\phi,l}(P_i)$, and (d) $\max_{\lambda,\phi,l}(P_i)$ as a function of f_{dip} . Filled and empty points indicate non-reversing and reversing simulations respectively. Orange shaded regions highlight plausible ranges of rapid changes as described in section 3.1. Stars indicate non-reversing simulations that contain global excursional events.

and Oceania (based on maps from LSMOD.2, see Korte et al. (2019b)), but $mean(P_i)$ remains below 0.5 for the duration of this event.

We define t_{ex} as the set of times between t_s and t_e over which a global or regional excursion occurs, i.e.

$$t_{ex} = t \in (t_s, t_e), \tag{15}$$

which is used when we consider mean and maximum values over only the time period of an excursional event, rather than a whole time series. For both global and regional excursions, we also define excursion duration Δt_{ex} (in years) as

$$\Delta t_{ex} = t_e - t_s,\tag{16}$$

where t_s and t_e are calculated from equations (13) and (14) for global and regional excursions respectively.

3. Results

3.1. Rapid changes and general variability

Fig. 1(a,b) show the fastest rates of virtual dipole strength and directional change in each of our simulations, calculated using $\max_{\lambda,\phi,t}(\mathrm{dM}_V/\mathrm{d}t)$ and $\max_{\lambda,\phi,t}(\mathrm{d}\hat{\mathbf{M}}_V/\mathrm{d}t)$ respectively, as a function of f_{dip} . M_V has been scaled to be compatible with the modern field as described in Davies and Constable (2018). Note that in Sections 3 and 4, rates of change and values of P_i have been calculated using a truncated $\ell_{max}=5$ as outlined in Section 2; the effects of using a truncation of $\ell_{max}=12$ will be considered in Section 4. Plausible ranges for the maximum rates of change are indicated by the orange shaded regions in each subfigure and are selected in light of the observational constraints discussed in Section 1: we chose $\max_{\lambda,\phi,t}(\mathrm{dM}_V/\mathrm{d}t)=0.3-3.0~\mathrm{ZAm^2~yr^{-1}}$ and $\max_{\lambda,\phi,t}(\mathrm{d}\hat{\mathbf{M}}_V/\mathrm{d}t)>1.5^\circ~\mathrm{yr^{-1}}$. For values of f_{dip} up to approximately 0.5, both reversing and non-reversing simulations are commensurate with observations of rapid changes. For cases with $f_{dip}>0.5$, the rates of change are generally too slow to match our selected observed ranges.

Fig. 1(c,d) show $\max_{\lambda,\phi,I}(P_i)$ and $\max_{\lambda,\phi,I}(P_i)$ for all simulations. The observed value of $\max_{\lambda,\phi,I}(P_i)$ is 0.1 over the past 100 ky (Panovska et al., 2019) and given the limited resolution of paleofield models this may well be a lower bound. Given the model uncertainties, we consider that simulated mean values should fall within the range 0.08 and 0.20. Simulations with $0.4 < f_{dip} < 0.5$ are consistent with this selected range for mean(P_i). In reversing simulations mean(P_i) can reach values up $\lambda \phi I$ to 0.5 in accordance with the behaviour of the dipole tilt, while simulations with $f_{dip} > 0.5$ have mean(P_i) that falls slightly below the observed range. There is a more marked transition in simulated behaviour when considering $\max(P_i)$, which ranges from 10-50 according to the field models (Panovska et al., 2019). Reversing simulations produce $\max_{\lambda,\phi,t}(P_i) > 100$, while simulations with $f_{dip} > 0.5$ produce $\max_{\lambda,\phi,t}(P_i) < 1$. The observed range of $\max_{\lambda,\phi,t}(P_i)$ is matched in simulations with $f_{dip} =$ 0.4 - 0.5. However, we should note that we cannot rule out that much larger maximum values might also be a feature of well-resolved reversing fields. 3 simulations with $f_{dip} = 0.4 - 0.5$ have $50 < \max(P_i) < 100$, resulting from M_V being close to zero at these points.

Fig. 1 shows that rates of change and PSV activity vary systematically with f_{dip} in this suite of dynamos. We have looked for trends between the paleomagnetic observables and the main dynamo control parameters (specifically Ra, Rm, E_{mag}/E_{kin} , Lehnert number $\mathcal{L}e = B/(\rho\mu)^{(1/2)}\Omega D$, and Rossby number Ro = RmE/Pm); most of these display little systematic variation, aside from some trend in $\mathcal{L}e$ and Ro (see supplementary material figures 1-5). There is evidence for greater field variability with increasing Ro, which we expect to reflect the increasing effect of inertia in the force balance. Based on the average values of Ro, inertia is 2 orders of magnitude weaker than the effects of rotation, indicating our simulations are in the rapidly-rotating regime. However Ro is higher than the equivalent value for the Earth, and so inertia plays a larger role in our simulations than is geophysically relevant. Trends could be obscured by the relatively small size of the dataset and our focus on high Rm QG-MAC dynamos. It might also be expected that paleofield behaviour is more reflective of dynamo behaviour at the CMB than integrated quantities such as Rm and Ro. Nevertheless, the results suggest that f_{dip} is a good proxy for the gross pale ofield behaviour found in current global models.

The results in Fig. 1 indicate that QG-MAC, high Rm dynamos with $0.4 < f_{dip} < 0.5$ simultaneously match the rapid directional and intensity changes and the general field variability observed in global timedependent field models spanning 0-100 ka. This range of f_{dip} is close to the dipole-multipole transition as defined by Christensen and Aubert (2006) and is consistent with previous suggestions that the geodynamo lies close in parameter space to this transition (e.g. Olson and Christensen, 2006). The range is also below the value of $f_{dip} = 0.65$ for the modern field, as might be expected given the present-day above average dipole moment. Although the time averaged value of f_{dip} lies in the range 0.4-0.5, when taking the maximum over the entire time series we find f_{dip} reaches values near 0.6, close to the modern field value. Simulations with lower f_{dip} can produce global excursions, and similarly simulations with high f_{dip} can produce regional excursions; however, we focus on the starred simulations in Fig. 1 given they are the ones that most closely match observed paleosecular variations.

Due to low resolution in paleomodels, f_{dip} is not well defined for paleomagnetic timescales. However, in our simulations, f_{dip} is strongly correlated with the axial dipole field strength. Ziegler et al. (2011) found the average axial dipole field strength over the past 2 My to be around 2/3 of its present day value. Lower values of f_{dip} would therefore be expected over this period compared to present day unless there was a commensurate decrease in the average non-axial dipole field, which is not suggested by the simulations. Similarly, Guyodo and Valet (1999) found from observational data that Earth's field becomes excursional when the intensity dipped to approximately half of that of the present-day dipole. When calculating f_{dip} from gufm1 (Jackson et al., 2000) with both a 1/3 and a 1/2 reduction in the axial dipole component, we find a decrease from $f_{dip} = 0.66 - 0.87$ to $f_{dip} = 0.51 - 0.76$ and 0.41 - 0.67 respectively, suggesting that our preferred range of f_{dip} is not implausible for times including geomagnetic excursions.

When considering the compliance criteria used by Christensen et al. (2010), we find all 20 of our dynamo simulations are at least marginally compliant with the modern field at various times over the course of the simulation (see Table A.1) i.e. the compliance rating χ^2 lies between 4 and 8. All non-reversing simulations exhibit marginal compliance for periods of at least 145 yr, with more strongly dipolar simulations featuring more extended periods of compliance. On average the simulations are not morphologically compatible with the modern geomagnetic field; however, we would not expect this to be the case given the enhanced variability and weaker dipole moment seen in the field models spanning the last 100 ky. It is also possible that necessary compromises in the simulation input parameters result in high values of χ^2 , though all of our non-reversing simulations lie within the morphologically compliant region of parameter space found by Christensen et al. (2010), with our reversing simulations close to the upper boundary. Ratings of $\chi^2 > 8$ indicating non-compliance are typically due to a low relative axial dipole power ratio AD/NAD and an overly high flux concentration factor FCF. Mean values for the AD/NAD ratio are below 0.75 in all 20 simulations, compared to the ideal value of 1.5 (Christensen et al., 2010), as might be expected due to the aforementioned weaker dipole moment. Mean FCF values are always above 3.25, often exceeding the compliant average value of 1.5 by several standard deviations. However, Christensen et al. (2010)'s ideal FCF value is estimated based on the historical field, with paleofield models lacking enough information to reliably calculate an equivalent FCF value for the paleomagnetic field. Otherwise, the other compliance criteria based on equatorial symmetry and zonality are close to their ideal values for the modern field.

Variations in P_i appear to mainly depend on f_{dip} , with $\underset{\lambda,\phi,t}{\operatorname{mean}}(P_i)$ falling by an order of magnitude when $f_{dip} > 0.4$, and $\underset{\lambda,\phi,t}{\operatorname{max}}(P_i)$ declining by three orders of magnitude over the range $f_{dip} \in (0.35,0.5)$. This suggests that simulations could be characterised in terms of P_i rather than f_{dip} , enabling closer comparison with paleomagnetic observational

data. Next we look in more detail at the properties of the excursions found in the simulations that match the paleofield observations in Fig. 1 (as indicated by stars).

3.2. Polarity excursions

Using the criteria defined in Section 2, we have found global excursions in 5 of our preferred simulations (i.e. those lying in the range $0.4 < f_{din} < 0.5$). Note that none of the other non-reversing simulations contained global excursions, although 2 other simulations that lie in the range $0.4 < f_{dip} < 0.5$ reach values of mean(P_i) ≈ 0.3 , indicating a global excursion may occur if the simulations were run for longer. Although our global excursions all occurred in simulations with $Ek > 2 \times 10^{-4}$, all but 2 of our simulations contained regional excursions (those being the two with the lowest choices of Ek, i.e. simulations LEDT019 and LEDT020). Fig. 2 shows the time series of $\max_{\lambda,\phi}(P_i)$, $\max_{\lambda,\phi}(P_i)$, $\max_{\lambda,\phi}(M_V)$, dipole tilt and energy ratios before, during, and after an example global excursion. An example of the field morphology at the midpoint of the excursion is also shown. In Fig. 2 (a), mean(P_i) exceeds 0.5 at approximately 7500 yr (where dimensional time has been calculated using equation (5)) and decreases below the threshold value of ≈ 0.1 around 10000 yr, marking the start and end of the global excursion respectively. During the global excursion mean(P_i) peaks at values around 2, whilst the max(P_i) reaches values of $\mathcal{O}(10^2)$. These changes in P_i arise from an increase of 36° in dipole tilt and 75% decrease in the mean(M_V), compared to their respective mean values over the entire time-series. The variation in $\mathop{\rm mean}_{\lambda,\phi}(M_V)$ during the simulated global excursion is comparable to the behaviour seen during the Laschamp excursion. Using predictions from GGF100K (Panovska et al., 2018b) and LSMOD.2 (Korte and Brown, 2019), mean(M_V) falls by around 94% and the dipole tilt increases by around 70° during the Laschamp excursion, so the simulated tilt is much less than in LSMOD.2. In Fig. 2 (d), the magnetic energy (normalised by its time-averaged value) decreases to around 60% during the global excursion, indicating a global change in field strength, while the kinetic energy (also normalised by its time-averaged value) remains relatively constant through the global excursion.

Fig. 2 also shows an example of a regional excursion. At around 14,000 yr, $\max_{\lambda,\phi}(P_i)$ briefly exceeds 0.5, while $\mathrm{mean}(P_i)$ remains at approximately the typical value of 0.1. The regional excursion has a short duration of ~185 yrs and is associated with both a decrease in $\mathrm{mean}(M_V)$ and increase in dipole tilt. However, these changes are within the normal variability of the field, similar to the Mono Lake excursion in which $\mathrm{mean}(M_V)$ falls by around 38% and the dipole tilt increases by 9°. Correspondingly, there is no clear change to the global energies during the regional excursion.

The example global excursion shown in Fig. 2 displays several features that are common to all global excursions in our simulations (see supplementary material figures 6-9), including a drop in $\max_{\lambda,\phi}(M_V)$ and relative magnetic energy and little change in relative kinetic energy. However, the behaviour of the dipole tilt varies across global excursions. Fig. 3 shows two further examples of global excursions that are characterised by lower mean(P_i) and $\max_{\lambda,\phi}(P_i)$ than the global excursion in Fig. 2. Compared to Fig. 2, the two global excursions in Fig. 3 show a greatly reduced dipole tilt variation of only 20°. Such a small tilt is not unusual in the context of the general simulation behaviour, and would be considered part of normal secular variation of the geomagnetic field. However, these global excursions are associated with a strong decrease in $\max_{\lambda,\phi}(M_V)$ that dictates the change in P_i and drives the field into an transitional state. It is also interesting to note that both global excursions in Fig. 3 have a longer duration than the global excursion in

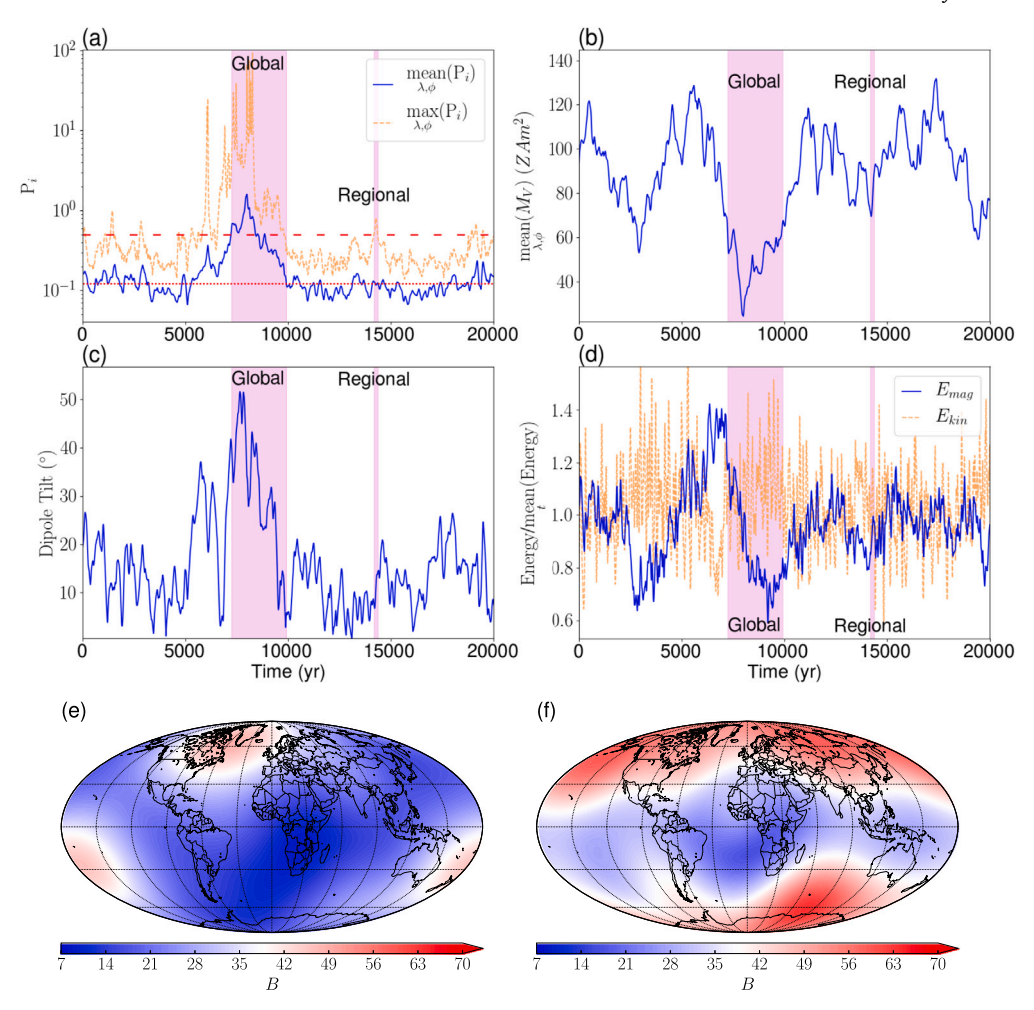


Fig. 2. Example global and regional excursional behaviour from simulation LEDS003. (a) $\max_{\lambda,\phi}(P_i)$ (solid blue) and $\max_{\lambda,\phi}(P_i)$ (dashed orange), (b) $\max_{\lambda,\phi}(M_V)$, (c) Dipole tilt, and (d) E_{mag} (solid blue) and E_{kin} (dashed orange), both normalised by their respective mean over the entire 150 ky time series, plotted as a function of time in years. Note that E_{mag} remains larger than E_{kin} throughout all of our non-reversing simulations. The shaded purple regions indicate the highlighted excursions. The red dashed line in (a) shows the critical values of P_i to determine t_s for global excursions and t_s and t_e for regional excursions as defined in equations (13) and (14) respectively (i.e. $P_i = 0.5$). The red dotted line shows the critical value of P_i to determine t_e for global excursions, as defined in equation (13). For clarity, a restricted and relabelled 20 ky range of time has been shown. (e) and (f) show the strength of the local field vector B at the surface at the midpoint of the global and regional excursions respectively.

Fig. 2 (approximately 5500 yrs and 5800 yrs respectively compared to 2500 yrs) despite having a lower activity.

Fig. 4 shows contour plots of $\max_{l_{ov}}(P_i)$, and the total amount of time within t_{ex} when $P_i > 0.5$ at each point (i.e. up to a maximum of Δt_{ex}), for the global (a, b) and regional (c, d) excursions shown in Fig. 2. In the global excursion $P_i > 0.5$ at all locations, with the largest values $(\mathcal{O}(10^2))$ around Southern Africa. This region is also where the longest total amount of time with $P_i > 0.5$ is seen, with the amount of time varying from around 500 to 2000 years, aside from two small patches in the northern hemisphere. These findings are consistent with LSMOD.2, which gives $P_i > 0.5$ at all locations. Note that despite the differences in dipole tilt highlighted above, maps like those in Fig. 4 for the global excursions shown in Fig. 3 exhibit the same general features; other global excursions show some variability, with P_i not always being greater than 0.5 at every point (see supplementary material figures 10-14). For the regional excursion shown in Fig. 4, P_i is only high in the mid-Atlantic, exceeding 0.5 for a total time of less than 500 yr, which is consistent with behaviour of the Mono Lake/Auckland excursion in LSMOD.2. We do not ascribe significance to the specific geographic variations of P_i and the excursion duration because there is no physical reason to expect that field behaviour would be anomalous in a particular location;

rather, these maps show global variations in field variability that are consistent with available paleofield models.

Previous paleomagnetic studies have suggested that excursions arise from a collapse of the axial dipole field, with the non-dipole field remaining relatively stable through the excursion (Brown et al., 2018; Panovska et al., 2019). Fig. 5 (a) shows mean(P_i) for the full time series of simulation LEDS003 (as seen in Figs. 2 and 4). Fig. 5 (b) shows the dipole component R_1 and the sum of the non-dipole components R_2 to R_{12} of the Lowes-Mauersberger spectrum calculated at the Earth's surface, as defined by

$$R_{l} = (l+1) \sum_{m=0}^{l} \left[(g_{l}^{m})^{2} + (h_{l}^{m})^{2} \right], \tag{17}$$

where g_l^m and h_l^m are the dimensionless gauss coefficients in the spherical harmonic representation of the radial field (e.g. Merrill et al., 1998). In (c), we further consider the power of the dipole component by plotting the axial dipole power $R_{1,1}^0$ i.e.

$$R_1^0 = 2(g_1^0)^2, (18)$$

and the equatorial dipole power R_1^1 , i.e.

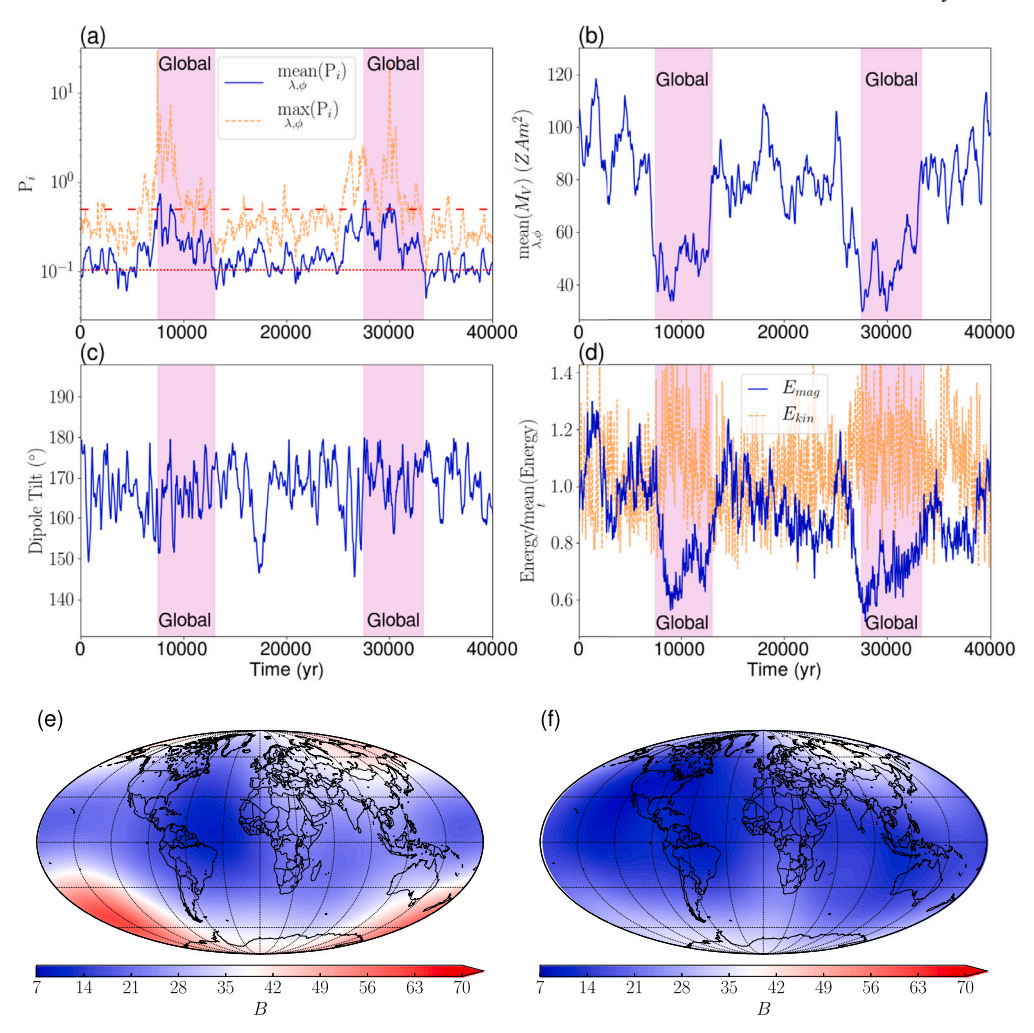


Fig. 3. Example global excursional behaviour from simulation LEDT004. Plots, dashed and dotted lines, and shaded regions are defined in the same way as in Fig. 2. For clarity, a restricted and relabelled 40 ky range of time has been shown. (e) and (f) show the strength of the local field vector *B* at the surface at the midpoint of the global and regional excursions respectively.

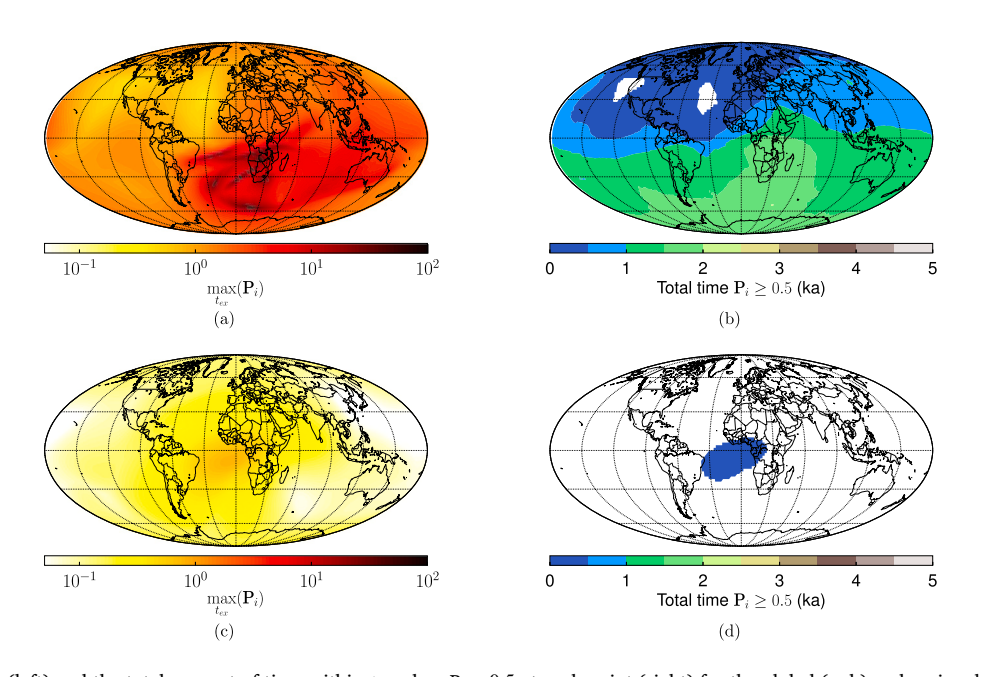


Fig. 4. Maps of $\max_{t_{ex}}(P_i)$ (left) and the total amount of time within t_{ex} when $P_i > 0.5$ at each point (right) for the global (a, b) and regional (c, d) excursions shown in Fig. 2. White regions indicate points where P_i never exceeds 0.5.

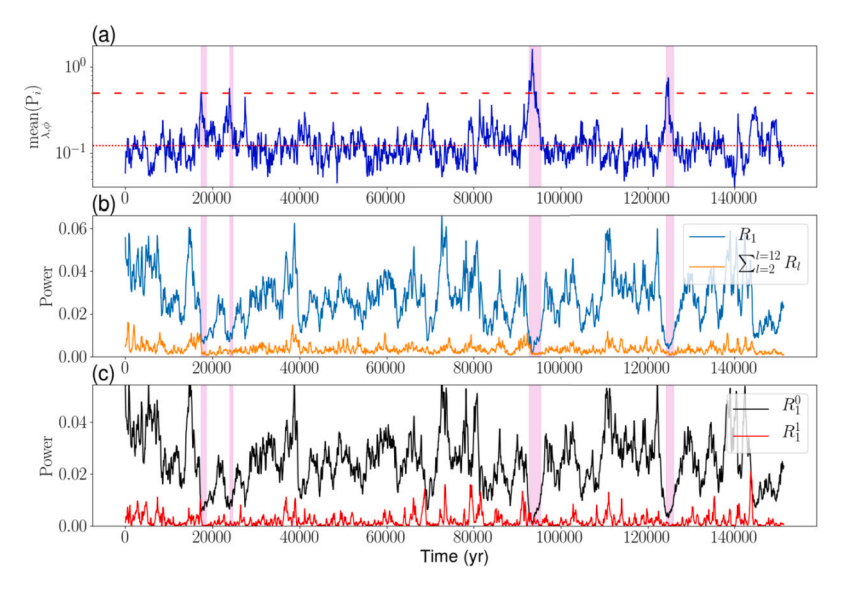


Fig. 5. (a) $\underset{\lambda,\phi}{\text{mean}}(P_i)$, (b) Lowes-Mauersberger spectra components R_1 (blue) and $\sum_{l=2}^{l=12} R_l$ (orange) and (c) R_1^0 (black) and R_1^1 (red) plotted as a function of time for simulation LEDS003. The shaded purple regions indicate the highlighted global excursions. The upper dashed and lower dotted red lines are defined in the same way as in Fig. 2.

$$R_1^1 = 2\left((g_1^1)^2 + (h_1^1)^2 \right). \tag{19}$$

During global excursions the g_1^0 component shows the largest fluctuations, with values closest to zero occurring at the corresponding times in which the mean activity index peaks. The equatorial dipole and non-dipole power appear to be relatively unaffected during the global excursions. Although there are occasional decreases (e.g. in the first and third excursions) in the equatorial dipole and non-dipole power, these are not systematic changes and it is clear that the power from the axial dipole is not going into the other components (based on the power spectra at the surface). This behaviour is consistent throughout all global excursions found in our simulations (see supplementary material figures 15-18). Therefore, the simulated results agree with paleomagnetic studies that global excursions reflect a collapse in the axial dipole field.

The correlation between the current weakening of the geomagnetic dipole field and the growth of a patch of reversed flux under the southern Atlantic (the South Atlantic Anomaly, SAA) has led to the suggestion that SAA-like features may be a potential signal of an incipient excursion or reversal (e.g. Terra-Nova et al., 2017). Similar recurrent features have been seen in Holocene paleofield models, though the relation to excursions has been disputed (Brown et al., 2018). Recurrence of such an SAA type non-dipole field feature can be represented by an increased eccentricity of an offset dipole (e.g. Nilsson et al., 2022). We see numerous increases in eccentricity throughout our simulations, which could reflect the emergence of SAA-like features. However, we do not find periods with increased eccentricity to systematically correlate with regional excursions.

4. Discussion

We have compared magnetic field morphology and variability in a suite of 20 dynamo simulations to global time-varying models of the paleomagnetic field spanning the last 100 ky. The simulations have been chosen to produce a QG-MAC balance (in the sense that magnetic/kinetic energy ratio exceeds 1) and a high magnetic Reynolds number of $Rm \sim 1000$ as expected for Earth's core. However, despite utilising a wide range of input parameters in our simulations, we are unable to access the geophysically relevant values of Ek, Pm, and Ra. Computational constraints prevent the use of the high resolution that would be necessary to capture the small temporal and spatial scales on the numerical grid, which is a consistent limitation for all direct numerical simulations of the geodynamo. Compromises on input parameter

values are also needed in order to run simulations for the requisite paleomagnetic timescales, to allow comparison with observational field models. However, within the limited parameter range explored we do not observe systematic variations of paleofield properties with dynamo control parameters. Instead, our simulations indicate that a dipolarity $f_{dip} = 0.4 - 0.5$ is crucial for obtaining synthetic field variability in accord with paleofield models.

Global time-dependent models of the last 100 ky are subject to their own limitations. Limited spatial and temporal resolution allows only large-scale features of the field to be resolved. Furthermore, selection of data used in observational models can be skewed towards certain areas and features, as the spatio-temporal sampling is uneven and samples used can be chosen based on implicit assumptions about reasonable field behaviour (Korte et al., 2019b). Such factors could potentially obscure observed excursional behaviour, which accentuates the need to build higher resolution models that can be further linked to dynamo simulations. In spite of these limitations, the GGF100k and LSMOD.2 models provide significantly better spatial sampling than that of previous models, and therefore provide the clearest views of rapid changes and excursional behaviour thus far. Furthermore, when calculating rates of change and P_i in our simulations using $\ell_{max} = 12$ instead of $\ell_{max=5}$, we find there are no significant changes in the results (see Table A.2), indicating the results may not be strongly resolution-dependent when considering $\ell_{max} \geq 5$.

We have used the activity index P_i of Panovska and Constable (2017) in order to quantify field variations in simulations and observational field models. The activity index accounts for changes in both field intensity and direction and so it is interesting to understand which of these factors is the primary influence behind global excursional events in dynamo simulations. Fig. 6 shows the maximum dipole latitude during our global excursions max(Dipole Latitude), plotted as a function of the ratio of the minimum $\stackrel{\iota_{\mathrm{ex}}}{M_V}$ during the excursion and $\underset{\lambda,\phi,l}{\mathrm{mean}}(M_V).$ Our global excursions have been plotted in order to compare with the activity index regime diagram shown in Figure 1 of Panovska and Constable (2017); here, the black line shows the expected values of dipole latitude and the M_V ratio for $P_i = 0.5$ using equation (10), with the intersection of the red dashed lines showing an excursion with a dipole latitude of 45° and a M_V ratio of 0.5. We see that the maximum dipole tilt (calculated from $90^{\circ}-\underset{\text{\tiny r}}{\text{max}}(\text{Dipole Latitude}))$ is usually between 20° and 40°, with only one excursion featuring a dipole tilt that exceeds 45° (as

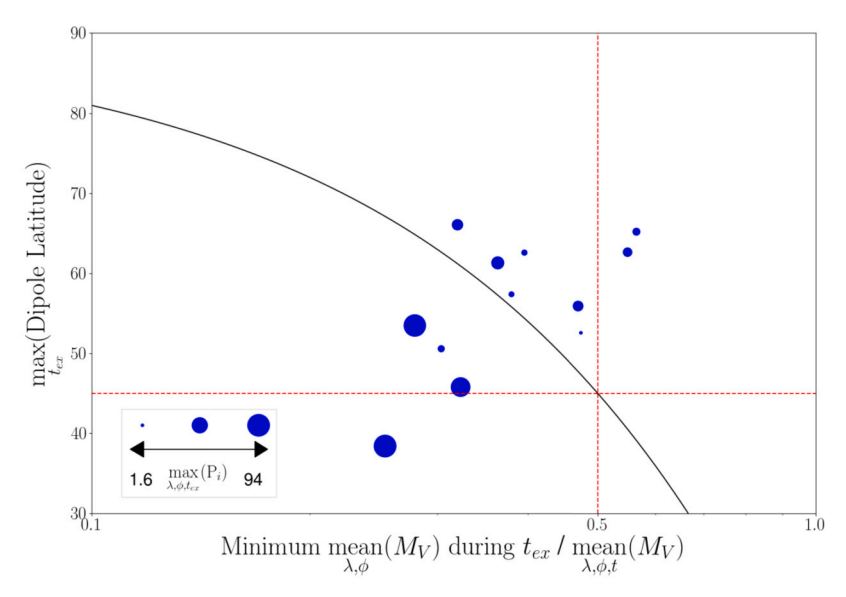


Fig. 6. Maximum dipole latitude plotted as a function of the ratio of the minimum M_V and $\max_{\lambda,\phi,i}(M_V)$ for all global excursions. The solid black line indicates values where $P_i = 0.5$. As in Panovska and Constable (2017), intersections of the red dashed lines represent the conventional limit used to characterize geomagnetic excursions, $P_i = 0.5$ and a maximum dipole tilt of 45°. The size of each point corresponds to $\max_{i,k,r}(P_i)$ for each excursion.

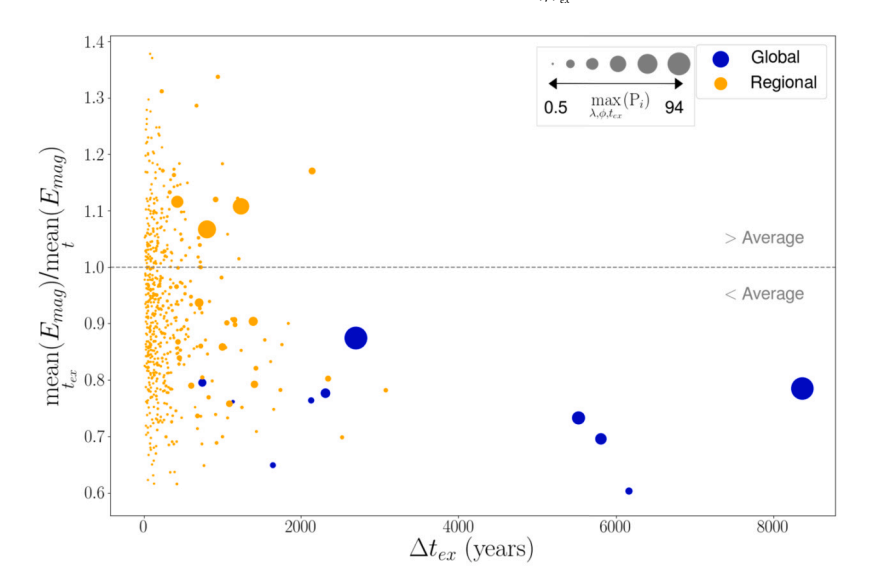


Fig. 7. Ratio of $\max_{t_{ex}}(E_{mag})$ and $\max_{t}(E_{mag})$ for each excursion plotted as a function of Δt_{ex} (in years). Blue and orange points indicate global and regional excursions respectively. The size of each point corresponds to $\max_{\lambda, \phi, t_{ex}}(P_i)$ for each excursion. The grey dashed line represents the average value of the magnetic energy ratio on the vertical axis.

shown in Fig. 2). The anomalous activity observed in our simulations is therefore due to a significant weakening of M_V (caused by the corresponding decrease in contribution from the axial dipole component), with the highest values of mean P_i occurring in correlation with the lowest values of the minimum M_V . By contrast the non-dipole field remains relatively constant during global excursions (Fig. 5) and so these events represent a collapse of the axial dipole field in our simulations.

Fig. 7 summarises the results from all global and regional excursions in our starred (Fig. 1) simulations in terms of the relative magnetic energy during an excursion, excursion duration, and the maximum value of P_i during the excursion. We see that there is no particular correlation between excursion duration and the maximum value of P_i , as large values of maximum P_i are obtained for short excursions (approx. 2000 yrs), and small values of maximum P_i are found for long excursions (approx. 6000 yrs). Both global and regional excursions produce a broad range of relative magnetic energies and durations, with the overlap between

the two ranges in the lower-left region of the figure indicating that they seem to occur within a continuous spectrum of variability, rather than global excursions being large anomalous events compared to the general variability of the field. Obtaining more global excursions in further simulations would potentially allow us to fill in the blank spaces in the lower half of the figure. We see that the longest regional excursions can be similar to shorter global excursions in terms of a decrease in the magnetic energy and maximum values of P_i. However, global excursions are always associated with an overall change in magnetic energy (as all lie below the average value of the magnetic energy) suggesting they are manifestations of global changes in the dynamo, and can last 2-3 times as long as the longest regional excursions. Despite this drop in the magnetic energy in global excursions, the dynamo remains in a strong-field state throughout as determined by δ remaining greater than 1. We find a decrease in δ during global excursions (due to an increase in inertia and decrease in the Lorentz force), but typically this is by about 10% to 40% of its mean value given in Table A.1. We found no systematic or significant changes in δ during regional excursions. The range and amount of regional excursions found in our simulations suggest that there may have been potentially many more excursions in the manner of the Mono Lake/Auckland excursion within the past 100 ky of Earth's field, that could be found via better spatial and temporal sampling in future observational models.

5. Conclusions

We have investigated a set of 20 numerical dynamo simulations with an Earth-like Rm and $E_{mag}/E_{kin}>2$ (indicating a QG-MAC force balance) that have been run for multi-millennial timescales, in order to compare the obtained field variations with those in the latest observational data. Our findings indicate:

- 1. Simulations with a QG-MAC force balance and high Rm are able to simultaneously reproduce rapid intensity and directional changes and the general variability observed over the last 100 ky. The paleosecular variation appears to depend on mean f_{dip} , as only the cases that lie within the range $0.4 < f_{dip} < 0.5$ are able to match both the rapid changes and the general variability simultaneously.
- 2. A wide spectrum of polarity excursions can be produced in dynamo simulations, ranging from short localized (<100 y) to mostly longer, global (up to 8 ky) events. Simulated global excursions are characterised by decreases in mean VDM and normalised magnetic energy, with such features having been observed in the Laschamp excursion.</p>
- Excursional events in our simulations occur due to a collapse in the axial dipole, with anomalous values of the activity index caused by a decrease in VDM rather than increased values of the dipole tilt.

Since we only have 10 global excursions in our models, further simulations that contain more excursions could usefully expand upon the range of variability we have observed. As the scope of this paper only covers comparing the features of excursions in observational models and numerical dynamo simulations, future work could also investigate the underlying mechanisms behind the range of simulated excursions. It will also be important to investigate the effects of stratification and core-mantle thermal interaction, following Mound and Davies (2023) who considered paleosecular variation in simulations with heterogeneous boundary conditions.

CRediT authorship contribution statement

Stephen J. Mason: Writing – review & editing, Writing – original draft, Visualization, Validation, Software, Methodology, Formal analysis, Conceptualization. **Christopher J. Davies:** Writing – review & editing, Writing – original draft, Supervision, Software, Project administration, Methodology, Funding acquisition, Conceptualization. **Andrew T. Clarke:** Software, Resources, Methodology. **Catherine G. Constable:** Writing – review & editing, Writing – original draft, Supervision, Project administration, Methodology, Funding acquisition, Conceptualization.

Declaration of competing interest

The authors declare that they have no known competing financial interests or personal relationships that could have appeared to influence the work reported in this paper.

Data availability

Data is available at https://earthref.org/ERDA/2744/, which contains the gauss coefficients used in all simulations.

Acknowledgements

We thank the reviewers for their positive reviews and helpful comments. We acknowledge support from two US National Science Foundation/UK Natural Environment Research Council grants (NSF references EAR 1953778 and EAR 2246758; NERC references NE/Y003500/1 and NE/V009052/1). Calculations were performed on the UK National supercomputing service ARCHER2.

Appendix A. Simulation results

Table A.1 Summary of input and output parameters for the simulations used in this paper. Output diagnostics are calculated using an untruncated value of l_{max} , i.e. using the full resolution of each simulation. From left to right: Case name, Ekman number Ek, Magnetic Prandtl number Pm, Rayleigh number Ra, Magnetic Reynolds number Rm, the fraction f_{ohm} of the total dissipation that is ohmic, Magnetic to kinetic energy ratio M, Lehnert number $\mathcal{L}e = B/(\rho\mu)^{(1/2)}\Omega D$, Non-dimensional simulation runtime t_* , Dimensional simulation runtime t_* (see equation (5)), time-averaged value of the compliance criteria parameter χ^2 (Christensen et al., 2010), minimum value of χ^2 over the entire time series, and time-averaged value of the strong field parameter delta (Schwaiger et al., 2019). Bold case names indicate simulations with global excursions, while an asterisk indicates a reversal containing reversals.

Case	E	Pm	Ra	Rm	f_{dip}	f_{ohm}	$\frac{E_{mag}}{E_{kin}}$	$\mathcal{L}e$	t_*	t (ky)	$\max_{t}(\chi^2)$	$\min_{t}(\chi^2)$	$\max_{t}(\delta)$
LEDS001*	0.001	50.0	480,000	1681.88	0.23	0.35	3.63	0.06	1.16	188	55.81	7.77	11.8
LEDS002	0.0004	35.36	1,200,000	1237.07	0.45	0.47	11.97	0.05	1.16	189	12.59	3.48	13.4
LEDS003	0.0004	50.0	1,750,000	2154.91	0.40	0.41	9.93	0.05	0.93	151	16.53	5.01	12.1
LEDT002*	0.001	35.36	480,000	1196.43	0.26	0.34	3.41	0.06	14.68	2386	42.83	5.47	10.1
LEDT003*	0.0005	25.0	1,920,000	1359.03	0.32	0.39	3.77	0.05	0.87	142	26.76	6.37	10.1
LEDT004	0.00025	17.68	7,680,000	1530.24	0.41	0.42	3.75	0.04	2.04	331	14.47	4.68	7.5
LEDT005	0.0002	15.81	12,000,000	1595.58	0.42	0.42	3.64	0.04	1.46	237	13.81	3.54	6.8
LEDT006	0.000125	12.5	30,720,000	1692.65	0.48	0.44	4.04	0.03	0.95	154	10.55	3.06	6.0
LEDT008*	0.001	35.36	360,000	974.32	0.35	0.37	5.55	0.06	5.18	841	25.11	4.78	10.8
LEDT009	0.0005	25.0	1,100,000	963.00	0.42	0.43	6.78	0.05	3.62	589	13.96	4.92	11.4
LEDT010	0.00025	17.68	3,360,000	957.29	0.46	0.49	7.78	0.04	4.25	691	11.79	2.11	12.5
LEDT013	0.0002	15.81	4,800,000	953.70	0.48	0.48	8.162	0.03	1.40	228	10.99	2.34	10.4
LEDT014	0.000125	12.5	10,080,000	927.00	0.51	0.53	9.38	0.02	0.90	146	9.52	2.63	11.6
LEDT015	0.0001	11.18	14,500,000	919.47	0.53	0.55	10.20	0.03	1.28	208	8.95	1.87	11.2
LEDT016	0.0000625	8.84	30,720,000	895.01	0.56	0.58	11.89	0.02	0.981	160	7.97	1.13	11.3
LEDT019	0.00003125	6.25	93,120,000	841.60	0.61	0.65	16.09	0.02	1.24	201	6.20	0.86	12.7
LEDT020	0.000015625	4.42	282,240,000	773.31	0.65	0.72	23.25	0.01	1.05	170	5.04	0.03	14.5
LEDT021	0.0001	12.0	19,200,000	1152.14	0.52	0.52	8.22	0.03	1.09	177	8.96	2.41	9.7
LEDT022	0.0001	7.0	38,400,000	1004.00	0.54	0.50	3.82	0.03	1.26	205	6.90	1.51	5.3
LEDT036	0.0000625	8.84	40,320,000	1037.42	0.56	0.56	9.50	0.02	0.96	157	7.63	1.66	9.7

Table A.2

Summary of rates of change for the simulations used in this paper. Output diagnostics are calculated using both a truncated $\ell_{max}=5$ and $\ell_{max}=12$ (brackets) as described in Section 2. From left to right: Case name, maximum rate of change of virtual dipole vector amplitude $\max_{\lambda,\phi,l}(\mathrm{dM}_V/\mathrm{d} t)$, maximum rate of change of virtual dipole position $\max_{\lambda,\phi,l}(\mathrm{dM}_V/\mathrm{d} t)$, maximum value of PSV index $\max_{\lambda,\phi,l}(P_i)$, and mean value of the PSV index $\max_{\lambda,\phi,l}(P_i)$. Note that the values of $\max_{\lambda,\phi,l}(P_i)$ are the same for both truncations, but differ when using more significant figures. Bold case names indicate simulations with global excursions, while an asterisk indicates a reversal containing reversals.

Case	$\max_{\lambda,\phi,t}(M_V)$	$\max_{\lambda,\phi,t}(\mathrm{dM}_V/\mathrm{d}t)$	$\max_{\lambda,\phi,t}(\mathrm{d}\hat{\mathbf{M}}_V/\mathrm{d}t)$	$\max_{\lambda,\phi,t}(\mathbf{P}_i)$	$\underset{\lambda,\phi,t}{\text{mean}}(P_i)$
LEDS001*	104.73 (106.27)	1.75 (1.92)	6.48 (6.39)	405.35 (478.55)	0.45
LEDS002	92.64 (93.44)	0.56 (0.59)	4.86 (5.13)	46.34 (18.90)	0.11
LEDS003	96.02 (96.70)	1.20 (1.10)	17.54 (19.65)	93.69 (216.15)	0.14
LEDT002*	100.50 (101.72)	1.41 (1.28)	3.20 (3.13)	749.35 (1021.83)	0.43
LEDT003*	96.80 (97.82)	0.92 (1.00)	4.18 (4.13)	307.88 (259.68)	0.30
LEDT004	92.54 (93.16)	0.65 (0.76)	4.67 (3.80)	29.53 (50.65)	0.12
LEDT005	91.94 (92.59)	0.76 (0.81)	6.21 (6.54)	57.13 (75.01)	0.11
LEDT006	90.36 (90.88)	0.68 (0.69)	3.79 (2.86)	16.85 (7.69)	0.09
LEDT008*	94.84 (95.81)	0.61 (0.66)	3.69 (3.64)	1002.47 (771.35)	0.36
LEDT009	92.26 (93.13)	0.51 (0.52)	3.87 (4.20)	91.38 (106.26)	0.12
LEDT010	90.42 (91.30)	0.43 (0.49)	1.73 (1.83)	15.24 (15.41)	0.10
LEDT013	89.28 (90.15)	0.42 (0.49)	0.61 (0.67)	1.33 (1.36)	0.09
LEDT014	90.15 (90.76)	0.37 (0.39)	0.58 (0.63)	1.27 (1.19)	0.08
LEDT015	88.42 (88.99)	0.34 (0.39)	0.49 (0.48)	0.73 (0.72)	0.08
LEDT016	88.02 (88.52)	0.32 (0.33)	0.48 (0.59)	0.63 (0.70)	0.08
LEDT019	88.83 (89.22)	0.26 (0.33)	0.36 (0.47)	0.45 (0.53)	0.07
LEDT020	90.99 (91.53)	0.28 (0.33)	0.25 (0.29)	0.47 (0.46)	0.06
LEDT021	89.39 (90.04)	0.56 (0.52)	0.60 (0.64)	0.59 (0.63)	0.08
LEDT022	90.28 (90.76)	0.34 (0.35)	0.43 (0.50)	0.55 (0.50)	0.07
LEDT036	89.72 (90.28)	0.35 (0.40)	0.42 (0.48)	0.72 (0.73)	0.07

Appendix B. Supplementary material

Supplementary material related to this article can be found online at https://doi.org/10.1016/j.epsl.2024.119011.

References

- Aubert, J., 2019. Approaching Earth's core conditions in high-resolution geodynamo simulations. Geophys. J. Int. 219, S137–S151. https://doi.org/10.1093/gji/ggz232.
- Aubert, J., Gastine, T., Fournier, A., 2017. Spherical convective dynamos in the rapidly rotating asymptotic regime. J. Fluid Mech. 813, 558–593. https://doi.org/10.1017/ jfm.2016.789.
- Ben-Yosef, E., Millman, M., Shaar, R., Tauxe, L., Lipschits, O., 2017. Six centuries of geomagnetic intensity variations recorded by royal Judean stamped jar handles. Proc. Natl. Acad. Sci. 114, 2160–2165. https://doi.org/10.1073/pnas.1615797114.
- Biggin, A.J., Bono, R.K., Meduri, D.G., Sprain, C.J., Davies, C.J., Holme, R., Doubrovine, P.V., 2020. Quantitative estimates of average geomagnetic axial dipole dominance in deep geological time. Nat. Commun. 11, 6100. https://doi.org/10.1038/s41467-020-19704-7
- Bono, R.K., Tarduno, J.A., Nimmo, F., Cottrell, R.D., 2019. Young inner core inferred from Ediacaran ultra-low geomagnetic field intensity. Nat. Geosci. 12, 143–147. https://doi.org/10.1038/s41561-018-0288-0.
- Brown, M., Korte, M., Holme, R., Wardinski, I., Gunnarson, S., 2018. Earth's magnetic field is probably not reversing. Proc. Natl. Acad. Sci. 115, 5111–5116. https://doi. org/10.1073/pnas.1722110115.
- Calkins, M.A., 2018. Quasi-geostrophic dynamo theory. Phys. Earth Planet. Inter. 276, 182-189. https://doi.org/10.1016/j.pepi.2017.05.001.
- Christensen, U.R., Aubert, J., 2006. Scaling properties of convection driven dynamos in rotating spherical shells and application to planetary magnetic fields. Geophys. J. Int. 166, 97–114. https://doi.org/10.1111/j.1365-246X.2006.03009.x.
- Christensen, U.R., Aubert, J., Hulot, G., 2010. Conditions for Earth-like geodynamo models. Earth Planet. Sci. Lett. 296, 487–496. https://doi.org/10.1016/j.epsl.2010.06.
- Constable, C.G., Davies, C.J., 2024. Rapid changes in strength and direction of Earth's magnetic field over the past 100,000 years. Geochem. Geophys. Geosyst. 25, e2023GC011236. https://doi.org/10.1029/2023GC011236.
- Davidson, P., 2013. Scaling laws for planetary dynamos. Geophys. J. Int. 195, 67–74. https://doi.org/10.1093/gji/ggt167.
- Davies, C., Constable, C., 2017. Geomagnetic spikes on the core-mantle boundary. Nat. Commun. 8, 15593. https://doi.org/10.1038/ncomms15593.
- Davies, C., Pozzo, M., Gubbins, D., Alfe, D., 2015. Constraints from material properties on the dynamics and evolution of Earth's core. Nat. Geosci. 8, 678–685. https://doi.org/ 10.1038/ngeo2492.

- Davies, C.J., Constable, C.G., 2014. Insights from geodynamo simulations into long-term geomagnetic field behaviour. Earth Planet. Sci. Lett. 404, 238–249. https://doi.org/10.1016/j.epsl.2014.07.042.
- Davies, C.J., Constable, C.G., 2018. Searching for geomagnetic spikes in numerical dynamo simulations. Earth Planet. Sci. Lett. 504, 72–83. https://doi.org/10.1016/j.epsl. 2018.09.037.
- Davies, C.J., Constable, C.G., 2020. Rapid geomagnetic changes inferred from Earth observations and numerical simulations. Nat. Commun. 11, 3371. https://doi.org/10.1038/s41467-020-16888-0.
- Dormy, E., 2016. Strong-field spherical dynamos. J. Fluid Mech. 789, 500–513. https://doi.org/10.1017/jfm.2015.747.
- Glatzmaier, G.A., Roberts, P.H., 1995. A three-dimensional self-consistent computer simulation of a geomagnetic field reversal. Nature 377, 203–209. https://doi.org/10.1016/0031-9201(95)03049-3.
- Guyodo, Y., Valet, J.P., 1999. Global changes in intensity of the Earth's magnetic field during the past 800 kyr. Nature 399, 249–252. https://doi.org/10.1038/20420.
- Jackson, A., Jonkers, A.R., Walker, M.R., 2000. Four centuries of geomagnetic secular variation from historical records. Philos. Trans. R. Soc. Lond. Ser. A 358, 957–990. https://doi.org/10.1098/rsta.2000.0569.
- Korte, M., Brown, M., 2019. LSMOD.2 global paleomagnetic field model for 50–30 ka BP. https://doi.org/10.5880/GFZ.2.3.2019.001.
- Korte, M., Brown, M.C., Gunnarson, S.R., Nilsson, A., Panovska, S., Wardinski, I., Constable, C.G., 2019a. Refining Holocene geochronologies using palaeomagnetic records. Quat. Geochronol. 50, 47–74. https://doi.org/10.1016/j.quageo.2018.11.004.
- Korte, M., Brown, M.C., Panovska, S., Wardinski, I., 2019b. Robust characteristics of the Laschamp and Mono Lake geomagnetic excursions: results from global field models. Front. Earth Sci. 7, 86. https://doi.org/10.3389/feart.2019.00086.
- Lhuillier, F., Hulot, G., Gallet, Y., 2013. Statistical properties of reversals and chrons in numerical dynamos and implications for the geodynamo. Phys. Earth Planet. Inter. 220, 19–36. https://doi.org/10.1016/j.pepi.2013.04.005.
- Liu, J., Nowaczyk, N.R., Panovska, S., Korte, M., Arz, H.W., 2020. The Norwegian-Greenland Sea, the Laschamps, and the Mono Lake excursions recorded in a Black Sea sedimentary sequence spanning from 68.9 to 14.5 ka. J. Geophys. Res., Solid Earth 125, e2019JB019225. https://doi.org/10.1029/2019JB019225.
- Livermore, P.W., Gallet, Y., Fournier, A., 2021. Archeomagnetic intensity variations during the era of geomagnetic spikes in the Levant. Phys. Earth Planet. Inter. 312, 106657. https://doi.org/10.1016/j.pepi.2021.106657.
- Maffei, S., Livermore, P.W., Mound, J.E., Greenwood, S., Davies, C.J., 2021. Fast directional changes during geomagnetic transitions: global reversals or local fluctuations? Geosciences 11, 318. https://doi.org/10.3390/geosciences11080318.
- Meduri, D., Biggin, A., Davies, C., Bono, R., Sprain, C., Wicht, J., 2021. Numerical dynamo simulations reproduce paleomagnetic field behavior. Geophys. Res. Lett. 48, e2020GL090544. https://doi.org/10.1029/2020GL090544.
- Merrill, R.T., McElhinny, M.W., McFadden, P.L., 1998. The Magnetic Field of the Earth: Paleomagnetism, the Core, and the Deep Mantle, vol. 63. Academic Press.

- Mound, J., Davies, C., Silva, L., 2015. Inner core translation and the hemispheric balance of the geomagnetic field. Earth Planet. Sci. Lett. 424, 148–157. https://doi.org/10. 1016/j.epsl.2015.05.028.
- Mound, J.E., Davies, C.J., 2023. Longitudinal structure of Earth's magnetic field controlled by lower mantle heat flow. Nat. Geosci. 16, 380–385. https://doi.org/10.1038/s41561-023-01148-9.
- Nakagawa, T., Davies, C.J., 2022. Combined dynamical and morphological characterisation of geodynamo simulations. Earth Planet. Sci. Lett. 594, 117752. https://doi.org/10.1016/j.epsl.2022.117752.
- Nilsson, A., Suttie, N., Stoner, J.S., Muscheler, R., 2022. Recurrent ancient geomagnetic field anomalies shed light on future evolution of the South Atlantic Anomaly. Proc. Natl. Acad. Sci. 119, e2200749119. https://doi.org/10.1073/pnas.2200749119.
- Ogg, J., 2020. Geomagnetic polarity time scale. In: Geologic Time Scale 2020. Elsevier, pp. 159–192.
- Olson, P., Amit, H., 2014. Magnetic reversal frequency scaling in dynamos with ther-mochemical convection. Phys. Earth Planet. Inter. 229, 122–133. https://doi.org/10.1016/j.pepi.2014.01.009.
- Olson, P., Christensen, U.R., 2006. Dipole moment scaling for convection-driven planetary dynamos. Earth Planet. Sci. Lett. 250, 561–571. https://doi.org/10.1016/j.epsl.2006. 08 008
- Olson, P., Driscoll, P., Amit, H., 2009. Dipole collapse and reversal precursors in a numerical dynamo. Phys. Earth Planet. Inter. 173, 121–140. https://doi.org/10.1016/j.pepi.2008.11.010.
- Olson, P.L., Glatzmaier, G.A., Coe, R.S., 2011. Complex polarity reversals in a geodynamo model. Earth Planet. Sci. Lett. 304, 168–179. https://doi.org/10.1016/j.epsl.2011.01.
- Osete, M.L., Molina-Cardín, A., Campuzano, S.A., Aguilella-Arzo, G., Barrachina-Ibañez, A., Falomir-Granell, F., Foix, A.O., Gómez-Paccard, M., Martín-Hernández, F., Palencia-Ortas, A., et al., 2020. Two archaeomagnetic intensity maxima and rapid directional variation rates during the Early Iron Age observed at Iberian coordinates. Implications on the evolution of the Levantine Iron Age Anomaly. Earth Planet. Sci. Lett. 533, 116047. https://doi.org/10.1016/j.epsl.2019.116047.
- Panovska, S., Constable, C., 2017. An activity index for geomagnetic paleosecular variation, excursions, and reversals. Geochem. Geophys. Geosyst. 18, 1366–1375. https://doi.org/10.1002/2016GC006668.

- Panovska, S., Constable, C., Brown, M.C., 2018a. Global and regional assessments of paleosecular variation activity over the past 100 ka. Geochem. Geophys. Geosyst. 19, 1559–1580. https://doi.org/10.1029/2017GC007271.
- Panovska, S., Constable, C., Korte, M., 2018b. Extending global continuous geomagnetic field reconstructions on timescales beyond human civilization. Geochem. Geophys. Geosyst. 19, 4757–4772. https://doi.org/10.1029/2018GC007966.
- Panovska, S., Korte, M., Constable, C., 2019. One hundred thousand years of geomagnetic field evolution. Rev. Geophys. 57, 1289–1337. https://doi.org/10.1029/2019RG000656.
- Panovska, S., Korte, M., Liu, J., Nowaczyk, N., 2021. Global evolution and dynamics of the geomagnetic field in the 15–70 kyr period based on selected paleomagnetic sediment records. J. Geophys. Res., Solid Earth 126, e2021JB022681. https://doi.org/10.1029/ 2021 JB022681
- Schaeffer, N., Jault, D., Nataf, H.C., Fournier, A., 2017. Turbulent geodynamo simulations: a leap towards Earth's core. Geophys. J. Int. 211, 1–29. https://doi.org/10.1093/gji/ggy/65
- Schwaiger, T., Gastine, T., Aubert, J., 2019. Force balance in numerical geodynamo simulations: a systematic study. Geophys. J. Int. 219, S101–S114. https://doi.org/10.1093/gji/ggz192.
- Shaar, R., Tauxe, L., Ron, H., Ebert, Y., Zuckerman, S., Finkelstein, I., Agnon, A., 2016. Large geomagnetic field anomalies revealed in Bronze to Iron Age archeomagnetic data from Tel Megiddo and Tel Hazor, Israel. Earth Planet. Sci. Lett. 442, 173–185. https://doi.org/10.1016/j.epsl.2016.02.038.
- Terra-Nova, F., Amit, H., Hartmann, G.A., Trindade, R.I., Pinheiro, K.J., 2017. Relating the South Atlantic Anomaly and geomagnetic flux patches. Phys. Earth Planet. Inter. 266, 39–53. https://doi.org/10.1016/j.pepi.2017.03.002.
- Wicht, J., Sanchez, S., 2019. Advances in geodynamo modelling. Geophys. Astrophys. Fluid Dyn. 113, 2–50. https://doi.org/10.1080/03091929.2019.1597074.
- Willis, A.P., Sreenivasan, B., Gubbins, D., 2007. Thermal core–mantle interaction: exploring regimes for 'locked' dynamo action. Phys. Earth Planet. Inter. 165, 83–92. https://doi.org/10.1016/j.pepi.2007.08.002.
- Ziegler, L., Constable, C., Johnson, C., Tauxe, L., 2011. PADM2M: a penalized maximum likelihood model of the 0–2 Ma palaeomagnetic axial dipole moment. Geophys. J. Int. 184, 1069–1089. https://doi.org/10.1111/j.1365-246X.2010.04905.x.